Supplementary Material: Melting Temperature, Emissivity, and Thermal Conductivity of Rare-Earth Silicates for Thermal and Environmental Barrier Coatings

Hunter B. Schonfeld[a,1], Milena Milich[a,1], Cameron Miller[b], Laura Doumaux[b], Mackenzie Ridley[c], Thomas Pfeifer[a], William Riffe[a], Davide Robba[d], Luka Vlahovic[d], Konstantinos Boboridis[d], Rudy J.M. Konings[d,2], Adam Chamberlain[e], Elizabeth Opila[b], Patrick E. Hopkins[a,b,f,*]

[a]*Department of Mechanical and Aerospace Engineering, University of Virginia, 122 Engineer's Way, Charlottesville, VA, 22904, USA*
[b]*Department of Materials Science and Engineering, University of Virginia, 395 McCormick Road, Charlottesville, VA, 22904, USA*
[c]*Oak Ridge National Laboratory, 1 Bethel Valley Road, Oak Ridge, TN, 37830, USA*
[d]*European Commission, Joint Research Centre, Hermann-von-Helmholtz-Straβe 1, Eggenstein-Leopoldshafen, 76344, Germany*
[e]*Rolls-Royce Corporation, 450 S. Meridian Street, Indianapolis, IN, 46225, USA*
[f]*Department of Physics, University of Virginia, 382 McCormick Rd, Charlottesville, VA, 22904, USA*

1. Sample Preparation

Twenty-two rare earth silicates were studied in this work including Sc, La, Lu, Y, Yb, (YYb), (YErYbLu), (ScYErYbLu), and (ScYGdDyErYbLu) disilicate [$RE_2Si_2O_7$], La, Nd, Gd, Yb, (LaGd), and (NdYb) monosilicate [RE_2SiO_5], and La, Nd, Gd, Yb, (NdCa), (LaGd), and (NdYb) stoichiometric apatite mixtures [$RE_{9.33}\square_{0.67}(SiO_4)_6O_2$]. The single component mono- and disilicate samples were synthesized beginning with high purity pre-reacted

*Corresponding author peh4v@virginia.edu
[1]Co-first authors
[2]Present address: Delft University of Technology, Faculty of Applied Sciences, Department of Radiation Science and Technology, Delft, 2628, Netherlands.

silicate powders (Praxair, United States), while the multi-component disilicates were created by mixing the appropriate ratios of their constituent single-component disilicate powders. Similarly, the stoichiometric apatites were created using a mixture of the single-component mono- and disilicate powders with a molar ratio of 5:2 respectively. Apatite formation was verified by x-ray diffraction (XRD). We note that the ytterbium apatite sample used for the melting point and emissivity measurements, however, remained unreacted upon sintering, resulting in a two-phase Yb_2SiO_5-$Yb_2Si_2O_7$ system at the start of the high-temperature measurements. Monosilicate and apatite samples were dry ball-milled for 24 hours before being cold pressed to 80 MPa. These were then annealed in a box furnace for 24 hours at 1600°C. Disilicate samples were dry ball-milled before being loaded into a 20 mm diameter graphite die and sintered via spark plasma sintering (SPS). These were sintered in argon at 65 MPa and at a maximum temperature between 1515-1625°C. Samples were then annealed in a box furnace at 1500°C in lab air for 24 hours to restore oxygen stoichiometry from the SPS process. XRD was conducted to confirm sample phase. For the disilicate samples studied which have multiple polymorphs, the β phase was formed and was stable at room temperature. The monosilicates were of the X1 or X2 phase depending on rare earth cation size, X1 for larger cations and X2 for smaller. Archimedes density was measured and found to be $\sim$96% dense for all the samples. Samples were polished to $<20\mu$m rms surface roughness for thermo-reflectance measurements. Post-melted samples were cross-sectioned, polished to 1 μm surface roughness, and mounted for qualitative scanning electron microscopy (SEM), energy dispersive spectroscopy (EDS), and 2D microfocus-XRD measurements.

2. Time-domain Thermoreflectance

Thermal conductivity measurements were conducted via time-domain thermoreflectance (TDTR) [1, 2, 3]. TDTR is an optical pump-probe technique commonly used to measure thermal conductivity in thin films and nanostructures. To facilitate this measurement, an 80 nm thin film of aluminum was deposited on the samples by electron beam evaporation to act as a transducer layer due to its desirable absorption and thermoreflective response at the laser wavelength. For TDTR measurements, we use a pulsed Ti:Sapphire laser with a center wavelength of 808 nm and a 80 MHz rep rate, split between a pump and probe beam path. While the pump is passed

through an electro-optic modulator (EOM) and modulated at 8.4 MHz, the probe is directed through a mechanical delay stage in order to vary the arrival time between the pump and probe pulse at the sample, allowing the transient thermal decay to be observed with picosecond resolution. The pump and probe beams are combined by a dichroic before being focused onto the sample by a 10X infinity-corrected objective lens. The resulting spot sizes at the sample surface have 20 μm and 10 μm $1/e^2$ diameters respectively, with a gaussian intensity profile. The reflected probe beam is then directed to a biased photodetector to monitor the transient change in reflectivity of the sample surface as a function of temperature induced by the pump heating event. The ratio of the in-phase and out-of-phase signals over time, as collected by a lock-in amplifier, is used to fit a multilayer thermal model of the axisymmetric cylindrical heat equation. We use this model to simultaneously fit for both thermal conductivity, k, and thermal boundary conductance (TBC), G, between the sample of interest and the thin metal transducer at the surface. The thickness of the aluminum was measured by picosecond acoustics on a sapphire reference sample, and its thermal conductivity was measured by four-point probe. The volumetric heat capacity of each sample was calculated via Neumann-Kopp rule of mixtures. This approach to estimating heat capacity has been previously validated near ambient conditions for a variety of mixed oxides by Leitner [4].

3. Melting Point Measurement

A laser heating and radiation pyrometry based technique, as previously described by Manara [5], was used to measure melting temperature and spectral emissivity *in situ*. In this technique a high power 4.5 kW Nd:YAG continuous wave laser was used to heat the sample surface while an array of pyrometers monitor surface radiance as depicted in Fig. 1a. The heating laser was focused down to a 3.5 mm diameter at the sample, with a uniform intensity. A flat beam profile was used to reduce thermal gradients within the measurement area, to ensure accurate pyrometer readings. A 256-channel spectro-pyrometer measured the intensity of radiated light from the sample surface from 500 nm to 1000 nm as the sample was heated through its melting point [Fig. 2a]. The spectro-pyrometer was calibrated using a tungsten lamp at 2500 K, and a calibration correction factor was calculated using the measured melting temperature of a molybdenum standard. Using the following derivation of Plank's equation, inverse radiance temperature, T, is

calculated at each wavelength, λ, for each time step:

$$\frac{1}{T} = \frac{\lambda}{C_2} \ln\left(1 + \frac{\frac{I_{cal}(\lambda)}{\tau_{cal}}}{\frac{I_{exp}(\lambda)}{\tau_{exp}}} (\exp \frac{C_2}{\lambda T_{rad,cal}} - 1)\right) \tag{1}$$

In Eq. (1), C_2 is the second radiation constant, $I_{cal}(\lambda)$ and $I_{exp}(\lambda)$ are the measured intensities of light radiated from the tungsten lamp and the sample at wavelength λ, respectively, and τ_{cal} and τ_{exp} are the time constants corresponding to those measurements. The 550-700 nm wavelength range was used to analyze the majority of the samples as the inverse radiance temperature linearly increases with wavelength within this range, allowing us to fit a linear parametric equation of the form $1/T = A + B\lambda$ to the spectral intensity data by a least squares approximation, as shown in Fig. 2b. The true temperature of the surface is thus the inverse of the y-intercept of the fit line, while the slope of the fit line is the spectrally averaged visible emissivity, ϵ(T). As long as the trend of inverse temperature and wavelength is linear in this range, the assumption of uniform spectral emissivity in the visible is valid. To improve our measurement precision, a faster, single wavelength pyrometer operating at 663 nm is also used to measure the radiance temperature with a 0.1 ms time constant over a 400 μm radius spot size on the sample. This allows us to capture the dynamic temperature changes at the surface with high temporal resolution seen in Fig. 1b. The real temperature of the sample surface, T, is then calculated from the measured radiance temperature, T_λ, by Wien's Law using the emissivity determined by the spectro-pyrometer:

$$T = [\frac{1}{T_\lambda} + \frac{\lambda}{C_2} \ln\left(\epsilon(\lambda, T)\tau(\lambda)\right)]^{-1} \tag{2}$$

The transmittance of the optical path at the pyrometer wavelength, τ_λ, is multiplied by the emissivity to account for losses through the sapphire chamber window.

At least 8 trials were conducted for each sample. These experiments were first run in 1.5 bar argon, followed by trials in ambient lab air. For the trials conducted in an inert atmosphere the chamber was iteratively pulled into vacuum and then filled with argon to reduce the amount of oxygen present. A slight positive pressure was applied during these trials to limit evaporation from the sample surface while it is heated. In each trial the sample is heated until melting occurs. After the sample is fully melted the laser is turned off and the material is allowed to naturally cool. We identify

the melting temperature through the resolidification point indicated by the temperature plateau observed during cooling. Although there may be some small hysteresis between the melting point and freezing point, we don't expect it to exceed the limits of our reported uncertainty. The true melting point is typically not observable during heating because the temperature rise is intentionally fast to limit silica volatilization and the melting transition is faster than that of solidification. On a few trials with a slower heating rate, however, we are able to identify the melting transition and observe that it is only slightly higher than that of the freezing point. The resolidification plateau generally offers a more consistent indicator of the solid-liquid phase transition, as it is without the influence of dynamic laser heating.

Laser heating was localized to an approximately 3.5 mm spot with a flat power distribution, allowing the sample to act as a self-crucible and thus minimizing undesired reaction with the graphite holding the sample in place. The graphite serves to thermally insulate the sample from the chamber, preventing large temperature gradients in the sample other than those induced by the laser. This both reduces the likelihood of sample fracture and reduces uncertainty in the pyrometer measurements by limiting the temperature variation within the measurement spot as much as possible.

As can be seen in the plots of measured melting temperature, the error bars of the measured melting temperatures are particularly large for samples with low emissivity or highly featured absorption spectra in the visible, such as in samples containing neodymium and erbium. This is the result of uncertainty propagation from fitting the inverse temperatures calculated from the spectro-pyrometer data with a linear fit to determine emissivity. The uncertainty associated with the 95% confidence intervals on this fit are propagated as the emissivity is used to calculate real temperature from the radiance temperature measured by the single-wavelength pyrometer. Neodymium sesquioxide and erbium oxide, however, have sharp absorption peaks in this wavelength range that lead to very large 95% confidence intervals for the linear fit. Since the multiple principal component disilicate samples have low emissivities and contain erbium, the resulting data points have very large error bars. We hope to reduce the uncertainty in these measurements in the future by applying a more advanced algorithm to the analysis that independently determines emissivity and temperature from spectrally-resolved pyrometer data.

4. Phase Stability

Additional analysis of the post-melt microstructure was conducted with SEM and XRD for samples that exhibited multiple thermal arrests during cooling. Four of the materials measured, the two-phase Yb apatite composition, $La_2Si_2O_7$, La_2SiO_5, and $(LaGd)_2SiO_5$ showed evidence of the resolidification of an additional phase through multiple thermal arrests. As previously discussed, we found that the Yb apatite sample had not reacted during its manufacturing and was still composed of its monosilicate and disilicate constituents. The higher resolidification temperature the Yb "apatite" mixture exhibited was 2285±50 K and the lower temperature resolidification occurred at 2203±57 K. The higher point corresponds to the melting of the Yb monosilicate phase and the lower to the disilicate, showing that we are able to determine these melting temperatures simultaneously during the experiment. All of the mono- and disilicates evaluated that included La showed evidence of phase separation. Interestingly, multiple arrests did not occur in any of the La-based apatites indicating phase separation did not take place. The two thermal arrests observed in the $La_2Si_2O_7$ sample were very similar in temperature and occurred at 2135±59 K and 2064±78 K. Through the morphological features present in SEM micrographs, we identify the formation of La apatite in the melt pool of the $La_2Si_2O_7$ sample, shown in Fig. 3a. The phase of the needle-like crystals is confirmed to be La apatite through micro-focus XRD (Fig. 3b). We believe the apatite formation was facilitated by the volatilization of silica from the laser melted region and the resulting shift in stoichiometry of the remaining liquid. Multiple thermal arrests associated were also observed in La_2SiO_5 and $(LaGd)_2SiO_5$ but occurred at temperatures lower than our spectro-pyrometer could reliably measure so true temperature values were unable to be determined. For La_2SiO_5 the secondary thermal arrest occurred at ∼1600 K radiance temperature and for $(LaGd)_2SiO_5$, its secondary resolidification occurred at around ∼1680 K with about 100 K standard deviation. These measured arrests occur nearly at the same radiance temperature and likely at the same true temperature since both materials have nearly equivalent emissivities. Interestingly, this resolidification point at ∼1600 K radiance temperature was not observed in $La_2Si_2O_7$.

Post-melt phase characterization was also conducted via SEM on the compositionally complex disilicate samples. The compositionally complex disilicates all had a single thermal arrest post melting, indicating that they

maintained single phase post melting. The five component disilicate, (Sc, Y, Er, Yb, Lu)$_2$Si$_2$O$_7$, had the one of the highest melting temperatures, showing promise for high temperature applications. The densified single phase is observed at the laser impingement point. EDS scans were completed down the center profile of the laser melt zone, providing the atomic percent of each element present at that point. These EDS measurements are consistent with an equimolar single phase solution of (Sc, Y, Er, Yb, Lu)$_2$Si$_2$O$_7$. The micro-focus XRD results support this EDS data, showing an equimolar single phase disilicate solution in the melt zone.

References

[1] C. A. Paddock, G. L. Eesley, Transient thermoreflectance from thin metal films, Journal of Applied Physics 60 (1986) 285–290.

[2] D. G. Cahill, Analysis of heat flow in layered structures for time-domain thermoreflectance, Review of Scientific Instruments 75 (2004) 5119–5122.

[3] A. J. Schmidt, X. Chen, G. Chen, Pulse accumulation, radial heat conduction, and anisotropic thermal conductivity in pump-probe transient thermoreflectance, Review of Scientific Instruments 79 (2008).

[4] J. Leitner, P. Chuchvalec, D. Sedmidubský, A. Strejc, P. Abrman, Estimation of heat capacities of solid mixed oxides, Thermochimica Acta 395 (2002) 27–46. doi:10.1016/S0040-6031(02)00177-6.

[5] D. Manara, . M. Sheindlin, . W. Heinz, . C. Ronchi, M. Sheindlin, W. Heinz, C. Ronchi, New techniques for high-temperature melting measurements in volatile refractory materials via laser surface heating, Rev Sci Instrum 79 (2008) 11.

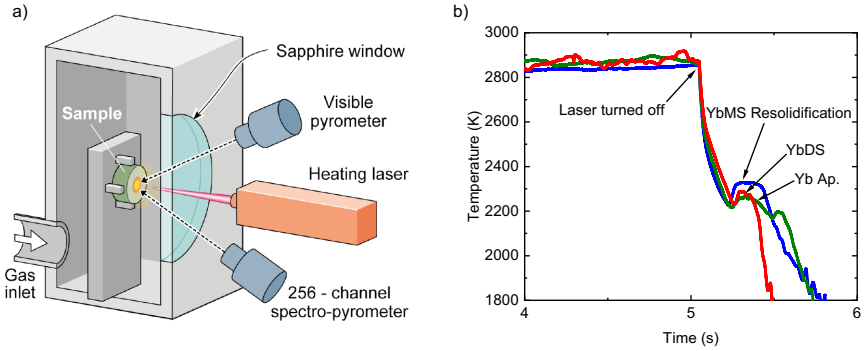

Figure 1: a) Schematic of laser and pyrometer configuration. b) Example of resolidification thermograms for Yb_2SiO_5, $Yb_2Si_2O_7$, and two-phase Yb_2SiO_5-$Yb_2Si_2O_7$ system.

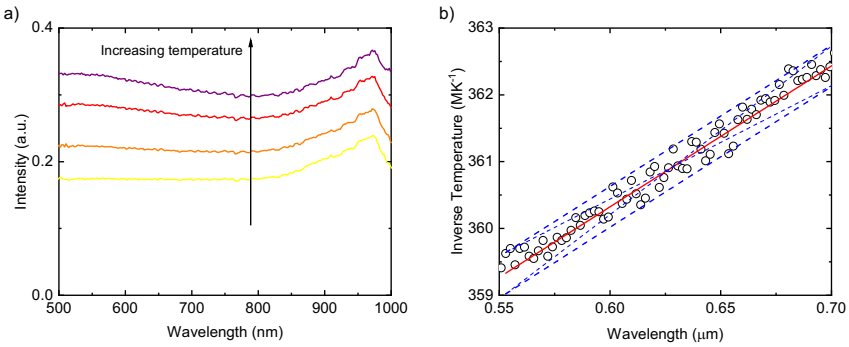

Figure 2: a) Raw spectral intensity data from spectro-pyrometer for $Yb_2Si_2O_7$. Distribution is affected by optical transmission and detector efficiency. b) Linear fit of spectral distribution of inverse radiance temperatures (black circles), including fit from 0.55-7 micron (red solid line) and 95% prediction interval (dashed blue line) used to determine maximum uncertainty in slope (dotted blue line).

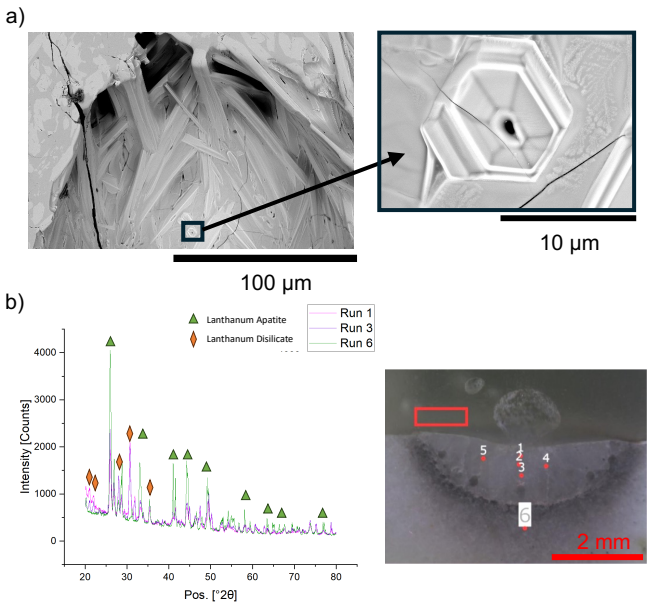

Figure 3: a) SEM characterization indicates the presence of two phases in the $La_2Si_2O_7$ sample after laser melting. The presence of an apatite phase is confirmed by micro-focus XRD (b).